Climatology of HF propagation characteristics at very high latitudes from SuperDARN observations

P. Ponomarenko[1] **and K.A. McWilliams**[1]

[1]University of Saskatchewan, Saskatoon, Canada

Key Points:

- Modelling HF propagation at very high latitudes is complicated by highly dynamic processes in the ionospheric plasma
- SuperDARN represents a convenient tool for direct observations of HF propagation characteristics
- SuperDARN interferometry data are utilised to build a climatological model of HF propagation

Corresponding author: Pasha Ponomarenko, pasha.ponomarenko@usask.ca

Abstract

Conventional forecasting of high-frequency (HF, 3-30 MHz) radio wave propagation is based on a combination of ionospheric and propagation models. However, at very high latitudes this approach is seriously undermined by the intrinsically dynamic ionospheric conditions regularly perturbed by energetic particle precipitations and strong electric fields. From this perspective, the multi-year observations of HF propagation characteristics by SuperDARN radars across auroral and polar cap regions represent a unique opportunity for systematic validation of the conventional approach, as well as for creating an empirical propagation model directly from the radar observations. Qualitative identification and quantitative characterisation of the propagation modes requires an accurate knowledge of the vertical angle of arrival (elevation angle) across the high-latitude part of the radar network. This information has become available only in recent years, facilitated by the development of reliable data-based calibration techniques for SuperDARN interferometry. We present the solar-cycle/seasonal/diurnal climatology of HF propagation characteristics at very high latitudes derived from two-frequency observations by the Rankin Inlet SuperDARN radar.

Plain Language Summary

High-frequency (HF, 3-30 MHz) radio waves are used for long-distance communication, navigation and surveillance purposes, as they can propagate over the horizon due to consecutive reflections from the ionosphere and the ground surface. The conventional forecast of HF propagation at mid and low latitudes relies on ionospheric models that are used to derive HF propagation characteristics. However, this approach becomes less reliable at auroral and polar cap latitudes due to the intrinsically high variability of the high-latitude ionosphere. In this work we lay an experimental foundation for an alternative propagation model based on direct observations of the HF propagation characteristics by Super Dual Auroral Radar Network (SuperDARN). This approach eliminates the necessity of using an ionospheric model by utilising accurate SuperDARN angle-of-arrival information obtained for a full solar cycle.

1 Introduction and problem formulation

Forecasting of high-frequency (HF, 3-30 MHz) radio wave propagation is conventionally performed using ionospheric models (e.g, IRI, Bilitza, 2018) and assumptions about HF propagation modes, like Breit and Tuve's Theorem (e.g., Davies, 1965). While this approach is generally reliable at low- and mid-latitudes, the intrinsically high variability of the high-latitude ionosphere represents a significant challenge in forecasting HF propagation in the auroral and polar cap regions. Progress has been made recently in modelling the high-latitude ionosphere through development of the Empirical-Canadian High Arctic Ionospheric Model (E-CHAIM), which is based on ionosonde observations poleward of 50 degrees geographic latitude and radio occultation of signals from the global navigation system satellites (GNSS) (Themens et al., 2017). However, a reliable high-latitude propagation forecast remains problematic as the principal propagation modes of the HF signals in these regions (E- and F-layer modes, low- and high-angle/Pedersen modes, multiple hops) are not well understood.

In this work, we will attempt to fill this gap by creating a solar cycle-long climatology of HF propagation modes at very high latitudes. Our approach is based on qualitative and quantitative characterisation of the principal propagation parameters of skip zone, virtual height and ground range, using observations from the Super Dual Auroral Radar Network (SuperDARN) (Greenwald et al., 1995; Chisham et al., 2007; Nishitani et al., 2019), which provides extensive coverage of the auroral and polar cap regions. Previous attempts to use SuperDARN to monitor HF propagation conditions (Hughes et al., 2002; Bland et al., 2014) were restricted to special operational regimes and utilised only echoes scattered by the ground surface (ground scatter, GS).

This work was made possible by recent breakthroughs in calibrating SuperDARN interferometry data with physics-based criteria (Ponomarenko et al., 2018; Chisham et al., 2021). Importantly, the physics-based calibration allows for post-processing of the data for which hardware information is either lost (historic data) or hard to obtain (remote sites). The essence of the proposed approach is that the accurate measurements of the vertical angle of arrival (elevation angle, α) of the radar backscatter echoes allows one to bypass an empirical ionospheric model and a theoretical HF propagation model. The calibrated elevation angle data remove the errors and uncertainties introduced by ionospheric and propagation models.

The well-understood dependence of the plasma refractive index on the electron density, N_e, also makes it possible to estimate N_e directly from the measured elevation angle values (Ponomarenko et al., 2011). Combining the group range and elevation angle provides virtual height estimates h_v, which pave the way for characterising the ground coverage (e.g., skip zone distance). Importantly, it is possible to extract useful HF propagation information from backscatter returns generated by the ionospheric irregularities (ionospheric scatter, IS). As there is a known correspondence between elevation angle and electron density, the dependence of elevation angle on virtual height at a fixed frequency is essentially equivalent to a conventional ionogram. This provides SuperDARN an opportunity to supplement E-CHAIM by filling gaps in ionosonde coverage at very high latitudes.

In this work we obtain information about the diurnal, seasonal, and solar cycle variations in the elevation angle of HF radar signals across the auroral and polar cap regions at two sufficiently different radar frequencies, $f \simeq 10$ and 12 MHz. This provides a solid foundation for building an empirical model of HF propagation at very high latitudes and represents an important step forward in improving the performance of communication and surveillance systems in these regions.

2 Radar operations and output data

SuperDARN represents the most advanced set of high-frequency (HF, working frequency range f=10-18 MHz) radars for studying ionospheric processes across mid to polar latitudes in both Northern and Southern hemispheres (Greenwald et al., 1995; Chisham et al., 2007; Nishitani et al., 2019). These radars typically scan once a minute through 16 azimuthal directions (beams) separated by 3.24°. Each beam is sampled at 70 to 110 group range cells (range gates) separated by 45 km in group range and typically spanning between 180 and 3,500-4,000 km in range. The data for each range gate are combined into autocovariance functions (ACF) which are integrated for $\simeq 3.5$ s. ACF phase is fitted with a linear function in order to estimate the Doppler frequency shift of the backscatter returns from decametre-scale ionospheric irregularities (Ponomarenko et al., 2021). The Doppler shift measurements are converted into line-of-sight (LoS) velocity values, which are then combined into maps of horizontal ionospheric $\mathbf{E}\times\mathbf{B}$ drifts. These maps are used to derive a large-scale spatial distribution of the electric potential across the auroral and polar cap latitudes, which is generated by the solar wind – magnetosphere – ionosphere (SMI) interactions (Ruohoniemi & Baker, 1998).

Essentially for the current work, almost all SuperDARN radars are equipped with two antenna arrays separated by $\simeq 100$ m along the boresight direction, which enables interferometric measurements of the elevation angle through measuring phase delay ϕ between the signals received by the two arrays (Milan et al., 1997). As elevation angle is directly affected by ionospheric refraction, its accurate measurement is very important in determining the propagation modes from its dependence on the group range (e.g., Ponomarenko et al., 2009). Furthermore, as the refraction coefficient of the ionospheric plasma depends on electron density N_e, the elevation measurements allow direct estimates of N_e in the scatter or reflection region of the ionosphere (Ponomarenko et al., 2011).

While SuperDARN interferometry data were available since the inception of the network in the early 1990s, they were rarely used due to the intrinsic difficulties with phase calibration of such large antenna arrays. This problem has been effectively resolved in recent years by designing physics-based algorithms to calibrate elevation angle measurements without requiring access to the hardware so that these algorithms can be applied to historical datasets (Ponomarenko et al., 2015; Burrell et al., 2016; Ponomarenko et al., 2018; Chisham, 2018; Chisham et al., 2021).

3 Dataset selection and data analysis details

The SuperDARN Canada radars at Saskatoon (SAS), Prince George (PGR), Inuvik (INV), Rankin Inlet (RKN), and Clyde River (CLY) are ideally suited for studying HF propagation at high and very high latitudes. They provide extensive coverage of the auroral (SAS, PGR) and polar cap (RKN, INV, CLY) regions. The analysed time interval covers the full solar cycle 24 (2008-2019 inclusive) for all sites except CLY, which began operating midway through year 2013. Another distinct feature of this dataset is that for most of the analysed period (late 2011 – early 2019) all radars were routinely operating in a two-frequency mode with carrier frequencies being alternated between 10-11 and 12-13 MHz every minute. Besides performing quasi-simultaneous ionospheric diagnostics at two sufficiently different frequencies, this regime also provides a considerably larger group range coverage as compared to the single-frequency mode.

We deliberately restricted the scope of the work presented here to illustrating the novel diagnostic capabilities of the SuperDARN radars to analyse the propagation modes of the HF signals based on accurate elevation angle measurements. We defer the derivation of a propagation model to subsequent studies. Furthermore, while an identical analysis has been performed for all five radar datasets, in this particular work we present the results only from the near-meridional beams of RKN radar covering auroral and polar cap latitudes.

The ACF data were converted into fitted parameters using the latest available version of the fitting software, FITACF3.0 (SuperDARN Data Analysis Working Group, 2021). This package differs from the previous versions in several aspects. The most relevant to this work are the following modifications:

- Fitted data pre-selection is based on a simple criterion – the signal-to-noise ratio is greater than 1 – in contrast to the complicated set of empirical criteria used in the preceding versions (Ponomarenko et al., 2022);
- Elevation angle is estimated directly from the cross-phase between signals received simultaneously by the main and interferometer antenna arrays, in contrast to fitting a linear function to phase from consecutive time lags of a cross-covariance function (XCF) between the time-lagged samples from these two arrays, which was implemented in the preceding versions of FITACF (Ponomarenko et al., 2021).

Calibration of the elevation angle data records consisted of determining a hardware time offset t_{diff} between the main and interferometer antenna arrays using an algorithm designed by Ponomarenko et al. (2018). Daily time offset values for the whole analysed interval 2008-2019 were estimated based on 24-hour datasets, each covering a UT day. Data at two frequency bands, 10-11 and 12-13 MHz, were analysed separately, thus producing two separate sets of daily t_{diff} values.

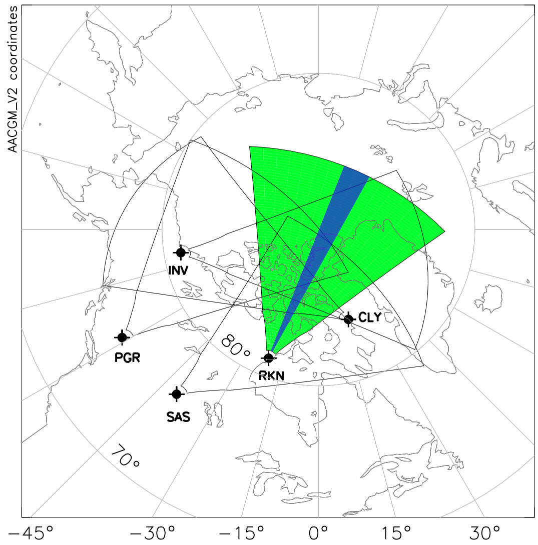

Figure 1. Fields of view (FoV) of SuperDARN Canada radars plotted in geomagnetic (AACGM-2) coordinates. In this paper we analysed data from beams 7 and 8 of Rankin Inlet (RKN). The approximate coverage is highlighted by blue within the RKN FoV, which is shown by green shading.

Typically, significant changes in t_{diff} due to hardware changes, faults or repairs appear as step-like 'jumps'. We produced t_{diff} *vs* time plots and inspected them visually to identify such occurrences, and each stationary (within a statistical uncertainty of 2-3 ns) interval between these 'jumps' was assigned a single offset value representing median of the daily t_{diff} values from within this interval. These offsets were entered into the SuperDARN metadata files that are used when processing SuperDARN ACF and XCF data. This will produce standard SuperDARN data files that contain well calibrated elevation angles.

The calibrated elevation angle values were used to build monthly two-dimensional histograms organized by group range and elevation angle, sorted by beam number and frequency band. Figure 2 shows examples of such histograms obtained for RKN near local noon (18-19 UT) for June 2013 across the nearly meridional beams 7-8 (blue shading in Figure 1). The top and bottom rows represent IS and GS components, respectively, and the left and right columns correspond to the 10-MHz and 12-MHz frequency bands. The IS and GS echo classification was performed using the conventional SuperDARN GS identification algorithm. GS echoes have distinctly lower values of spectral width and LoS velocity (for more detail see, e.g., Subsection 4.1 in Ponomarenko et al., 2007). Each distinct contiguous grouping of high occurrences (i.e., a 'patch') in these plots corresponds to a distinct propagation mode.

After assessing the feasibility of different methods to characterise the 'mean' elevation angle at a given range gate, we concluded that the optimum approach is based on the following considerations and steps:

- Instead of using the distribution $\alpha(r)$, we used the interferometer phase Ψ as the primary measured parameter. This avoids misinterpretation of different echo populations caused by a highly non-linear conversion between Ψ and α at very low elevation angles (for more detail, we direct the reader to Subsection 4.1.1).

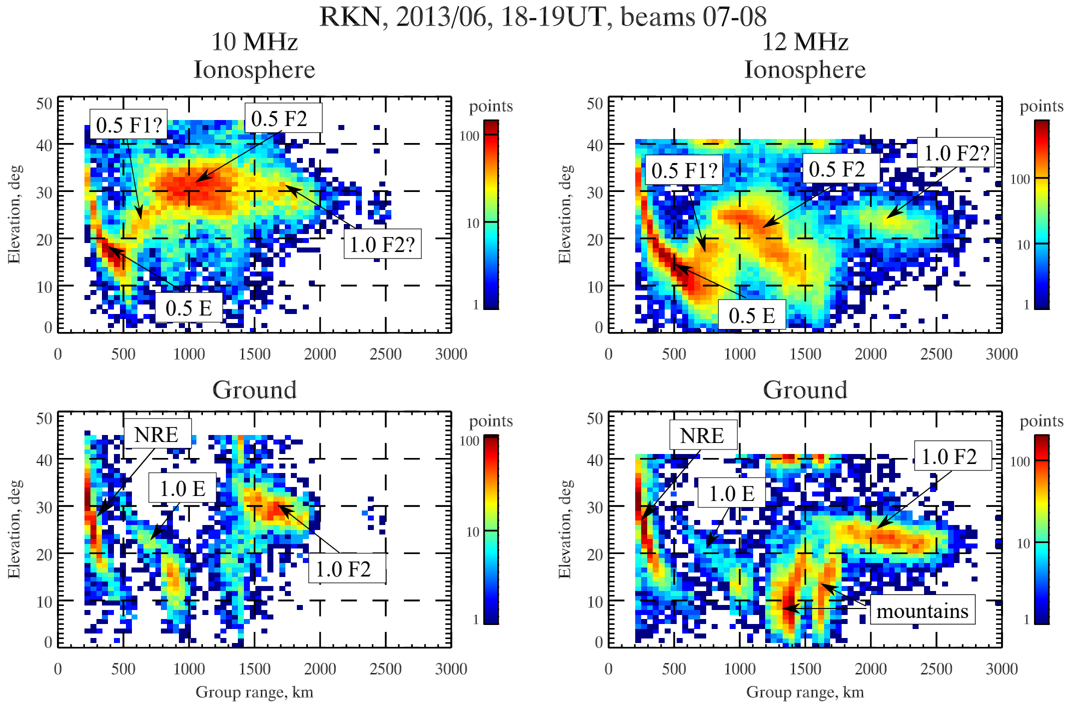

Figure 2. Example of group range – elevation angle histograms for RKN beams 7-8, in June 2013 at 18-19 UT. Top row: ionospheric scatter (IS), bottom row: ground scatter (GS). Left column: 10-MHz frequency band, right column: 12-MHz frequency band.

- For each range gate, a phase Ψ histogram was calculated in the same way as the elevation angle histograms. The bin width of $8°$ was selected empirically based on a trade-off between the acceptable phase resolution and statistical reliability.
- For each range gate, we assigned a single value of phase, Ψ_{max} which corresponds to the maximum of the respective histogram. If there were less than 10 data points in the respective histogram bin, no Ψ_{max} value was assigned to this range gate.
- The obtained dependencies $\Psi_{max}(r)$ were converted into 'mean' elevation angle values $\bar{\alpha}(r)$ and passed to further analysis.

It is necessary to mention that, while this approach avoids errors related to calculating a single mean value for a multi-peak histogram, its downside is that it characterises only one propagation mode even if multiple components with distinctly different values of $\bar{\alpha}$ overlap in group range. We leave the significant problem of decoupling these components to future work.

4 Visual identification of HF propagation modes and their quantitative characterisation

4.1 Seasonal-diurnal variability

The two principal propagation modes–Pedersen and low-angle–can be separated based on how the elevation angles behave with range (e.g, Subsection 4.3.1 in Davies, 1965). Low-angle echoes are characterised by elevation angle decreasing with group range, while the Pedersen echoes have elevation angle remaining essentially constant with r (e.g., Figure 3 in Ponomarenko et al., 2009). Different 'hops' of the same propagation mode can be identified by analysing the relationship between the distance from the radar to the near edges of different propagation populations, r^{min}. For example, for the two-hop and one-hop modes of GS echoes, the ratio between their r^{min} values should be approximately 2, while the r^{min} ratio for the 1.5-hop and 0.5-hop IS components should be closer to 3.

4.1.1 Summer data

As an example of the analysis that was done for all the data, let us analyse the midday summer data from Figure 2. In the 10-MHz IS data (top left) the ‘blob’ at $r \leq 500$ km corresponds to the low-ray 0.5-hop E-layer echoes while a ‘patch’ between 700 and 1,500 km centred at $\alpha \simeq 30°$ is produced by the F2-layer 0.5-hop Pedersen-mode returns. The ‘isthmus’ connecting these two areas seems to be related to the F1-layer ‘ledge’, although it may also result from interference between E- and F-layer echoes overlapping in group range.

The 10-MHz GS data (bottom left) show three distinct populations: so-called near-range echoes (NRE, Ponomarenko et al., 2016) at $r \leq 300$ km, 1-hop E-layer echoes ($r \simeq 500-1000$ km), and 1-hop F2-layer echoes ($r \simeq 1400-1900$ km). NRE are scattered by the lower part of the E-layer at $h \simeq 100$ km (Ponomarenko et al., 2016). As these echoes are not affected in any significant way by ionospheric refraction, they seem to be produced by isotropic rather than field-aligned irregularities of electron density, in contrast to the conventional E-layer backscatter. The NRE populations are misidentified as GS returns by the conventional SuperDARN algorithms due to their relatively low values of LoS velocity and spectral width. Furthermore, from comparing IS and GS histograms, the ’tail’ following the 0.5-hop Pedersen IS population at $r \simeq 1500-2000$ km seems to be produced by some of the 1-hop GS echoes being misidentified by the conventional software as IS returns. Finally, the apparently low occurrence of the E-layer GS echoes is most probably because they are obscured by 0.5-hop F-layer IS returns coming from the same group ranges.

As expected, the 12 MHz data in (right panels) show lower elevation angle values and larger group ranges for the F-layer echoes as they experience weaker ionospheric refraction as compared to that for the 10 MHz echoes (left panels). In contrast to the 10-MHz data, the 0.5-hop F2 component in the (top right) represents a combination of both Pedersen (constant elevation angle) and low-angle (elevation angle decreasing with r) modes. Furthermore, the 12-MHz GS data (bottom right) show two bands of echoes across $r \simeq$1300-1700 km at $\alpha \leq 20°$ whose elevation increases with group range. This cannot be explained within the conventional concepts of either Pedersen or low-angle propagation modes. However, a more in-depth analysis reveals that these populations correspond to E-mode GS echoes from mountain ranges in the southern parts of Devon and Ellesmere Islands in the Arctic Archipelago (see Figures 4 and 5 in Ponomarenko et al., 2010). As each such area represents an effective target fixed in physical range, with decreasing electron density or increasing the layer’s height their echoes would need to travel at higher elevation angles and for longer time causing increase in their group range.

The dominance of Pedersen regime in the F-layer modes is caused by the presence of a regular photoionisation E-layer, which effectively blanks the low-ray mode from reaching the F-layer altitudes. To illustrate this effect, in Figure 3 we show results of ray-tracing simulation for a single Chapman-type F-layer (a) and the same F-layer but in combination with an E-layer (b). In this Figure, the simulated ionospheric properties and the radar frequency value are listed in the panel headings. The radar is located at the origin of the Cartesian coordinates. The magnetic field inclination with respect to the Earth’s surface is 85° towards the radar. The blue-white background depicts the distribution of the plasma refractive index n, with darker blue corresponding to a larger deviation from unity. While the full form of the Appleton-Hartree equation describing plasma refractive index is quite complex (e.g., Davies, 1965), for frequencies near $f \geq$10 MHz one can

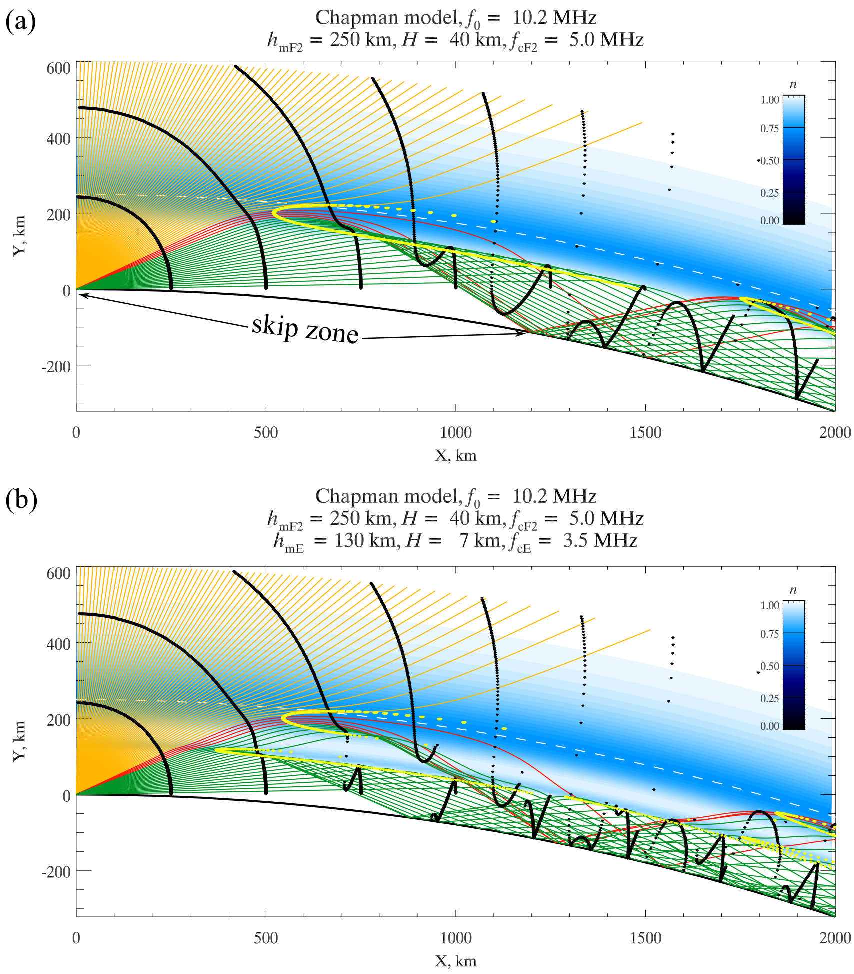

Figure 3. Ray tracing simulations of HF propagation trough (a) a single F-layer and (b) a combination of F- and E-layers (see text for details).

neglect the effects of ion-neutral collisions and the magnetic field. In these simulations, a simplified form of the Appleton-Hartree equation has been utilised for calculating n:

$$n^2 = 1 - \frac{f_p^2}{f^2}, \tag{1}$$

Here f_p is the 'plasma frequency,' which is given by:

$$f_p = \sqrt{\frac{e^2 N_e}{4\pi^2 \epsilon_0}} \tag{2}$$

where e is the electron charge and ϵ_0 is the permittivity of free space.

The ray-tracing simulations were run with a spatial resolution of 1 km along the ray and 0.1 ° in elevation angle, but only rays corresponding to integer elevation angle values are plotted. The orange, red and green traces correspond to escaping, Pedersen and low-angle rays, respectively. The yellow contour represents regions where the rays are nearly orthogonal to the geomagnetic field, thus providing optimal conditions for HF backscatter from the field-aligned irregularities of electron density. Black lines show contours of equivalent group ranges in 250-km steps, and the white dashed line shows the location of the F-layer maximum. These simulation results also explain the relatively narrower elevation angle extent in 1-hop F2 component as compared to that for 0.5-hop because the escaping rays (orange) scattered from higher elevation angles contribute to the 0.5-hop IS component only but do not affect any GS echoes as they never reach the Earth's surface.

It is clear that in panel (b) most of the low-angle rays are trapped between the E-layer and the ground, and only few of them reach the F-layer. This effect should be more pronounced at lower radar frequencies, as they experience comparatively more refraction under fixed ionospheric conditions. This means that on some occasions the E-layer maximum density is high enough to block most of the low-angle rays at 10 MHz, but it is insufficient to do the same at 12 MHz. This might explain the combination of both Pedersen (horizontal) and low-ray (descending) 'patches' observed in the IS F-mode at $f \simeq 12$ MHZ, while the respective 10-MHz data show Pedersen component only.

Another important detail is that in the panels on the right there are some patches of very high elevation echoes $\alpha \simeq 40°$ in the 12-MHz data that are seemingly unrelated to other echo populations. These patches represent a known artifact caused by the statistical fluctuations in the interferometer phase that triggers a random 2π adjustment in signals coming from very low elevation angles. For more detail, see Figure 5 and the related text in (Ponomarenko et al., 2018). This artifact is effectively concealed by the highly non-linear conversion of the interferometer phase difference Ψ into the elevation angle at $\alpha \to 0$ so that a single population split into two parts through the 2π ambiguity in the phase domain will look as two apparently unrelated populations in the elevation angle domain (see, e.g., Figure 2 in Ponomarenko et al., 2015). To identify such cases, alongside the elevation angle histograms, we inspected the respective phase histograms as well. The efficiency of utilising interferometer phase to eliminate this artifact is illustrated in Figure 4. Panel (a) replicates the GS elevation-range histogram at 12 MHz from Figure 2, while panel (b) shows the corresponding histogram of *adjusted phase* (see (Ponomarenko et al., 2018) for its definition). The black diamonds in panel (a) show locations of peaks of elevation angle histograms. The red rectangle shows the peaks at very high elevation angles produced by the above artifact. The white line in panel (b) shows histogram peaks in interferometer phase which are free from these 'jumps.' The elevation angle values calculated from the phase histogram peaks,$\bar{\alpha}$, are plotted in panel (a) by the white line, which accurately follows the elevation histogram peaks but eliminates the 2π ambiguity distortions.

To illustrate diurnal trends, in Figure 5 we show a group range *vs* UT map of the 'mean' elevation angle values $\bar{\alpha}$ for data from RKN beams 7-8 during the month of June

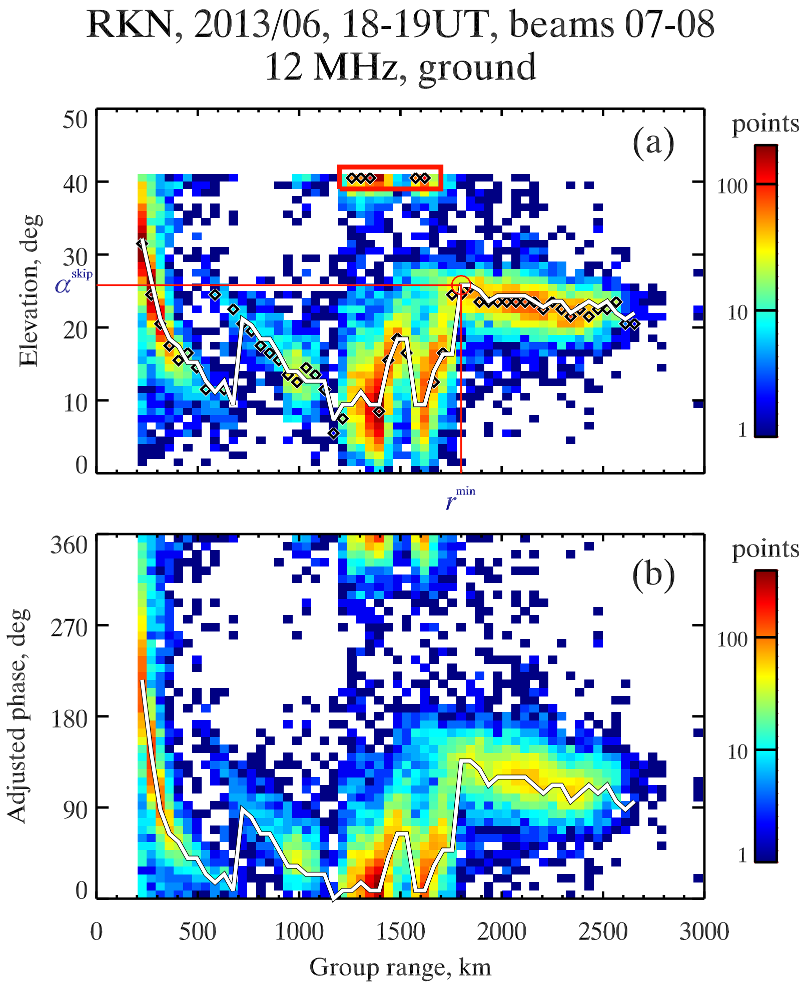

Figure 4. Ground stater group range – elevation angle (a) and group range –interferometer phase (b) histograms at 12-MHz frequency band for RKN beams 7-8, in June 2013 at 18-19 UT. Black diamonds in panel (a) show peaks of elevation angle histograms at each range gate. The white line in panel (b) shows peaks of interferometer phase histograms, while the white line in panel (a) shows elevation angle values calculated from the interferometer phase peaks (see Subsection 4.1.1 for details). The red circle and red lines in panel (a) indicate the skip zone boundary for 1.0-hop F-layer mode, characterised by group range r^{min} and elevation angle α^{skip} (see Subsection 5.3 for details).

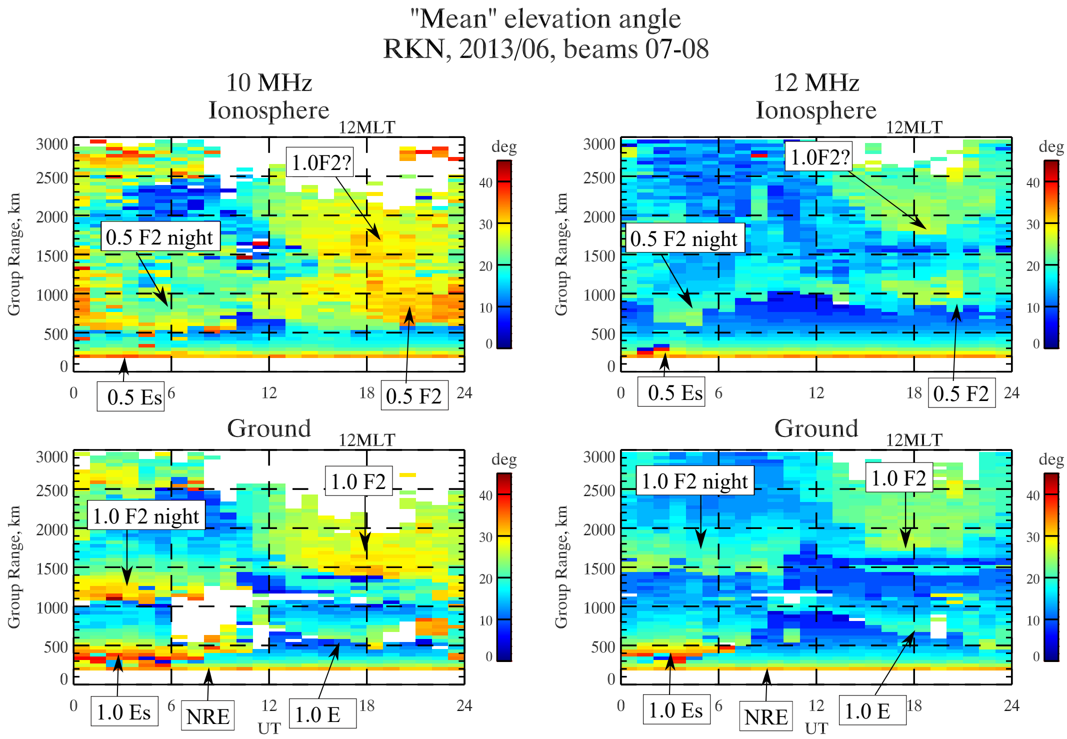

Figure 5. Group range-UT map of 'mean' elevation angle values $\bar{\alpha}$ (see Section 3 for details) in RKN beams 7-8 for June 2013. The local magnetic/solar noon for these nearly meridional beams is close to 18 UT.

2013. The panels in this figure correspond to the same components as the respective panels in Figure 2. For convenience of visual analysis, at the top of each panel we marked an approximate position of local magnetic noon, 12 MLT ($\simeq$ 18 UT) along the beams' directions. Fortuitously, the magnetic and geographic local times along those beams coincide within a one-hour bin. In addition to the daytime modes identified in Figure 2, between 0 and 12 UT (18-06 MLT) there are two nighttime components arising from a sporadic E layer, E_s, at close ranges, $r \leq 500$ km, and a nighttime F2 layer at farther distances. In contrast to the daytime observations, the nighttime F2 propagation modes in both IS and GS show $\bar{\alpha}$ decreasing with r, which is characteristic of the low-angle rays. This difference most probably results from the semi-transparent (patchy) nature of E_s, which allows the low-angle rays to penetrate to the F2 layer altitudes, while the regular daytime E-layer provides a 'blanket' for these rays.

The plots show distinct diurnal trends for different propagation modes that generally agree with the conventional understanding of day-night variations in ionospheric parameters. For example, as the maximum electron density in both regular (photoionisation-induced) E- and F-layers maximises close to the local noon, the corresponding $\bar{\alpha}$ values increase while the scatter regions move closer to the radar (r decreases). Furthermore, as expected, the same propagation modes come from more distant group ranges and exhibit lower $\bar{\alpha}$ values in the higher frequency band (right panels in Fighure 5).

4.1.2 Winter data

The diurnal variations in $\bar{\alpha}$ for December 2013 are shown in Figure 6. In contrast to the summer data, the daytime F2 propagation in winter is dominated by the low-angle mode represented by 0.5-hop and 1.5-hop modes in IS (top panels) and by a 1-hop mode in GS (bottom panels). For this mode the maximum elevation angles and, therefore, the maximum plasma frequency are noticeably higher than those for the summer data, reflecting the well-known effect of the winter anomaly when the winter daytime values of the F-layer electron density are noticeably larger then those observed during the summer months (e.g., Yonezawa, 1971). It is necessary to point out that the daytime population in GS data between 16 and 21 UT ($\simeq 10-15$ MLT) most probably represents the 0.5-hop F2 mode misidentified by the conventional software as GS due to its relatively low LoS velocity and narrow spectral width. At this stage, we consider two possible causes of this population of IS echoes being misidentified as GS. First of all, due to elevated f_p values the radar signals experience a strong refraction so that the effective scatter volume is shifted to within $r \simeq 300 - 500$ km from the radar site. What is important here is that under average geomagnetic conditions $2 \leq K_p \leq 3$ this area lies equatorward of the outer auroral oval boundary normally located at $\simeq 75-79°$ MLAT (see, e.g., Figure 4 from Carbary, 2005). As has been shown by, e.g., (de Larquier et al., 2013), the sub-auroral IS echoes are usually characterised by relatively low values of both spectral width and LoS velocity so that most of them would be routinely labelled as GS. This effect is enhanced by the comparatively low values of the ionospheric refractive index at the scatter areas, which further lowers the apparent LoS velocity values (Ponomarenko et al., 2009).

While the winter data are obtained from the nominal polar cap, where there is no direct sunlight reaching the ground, the daytime F2 returns are still provided by the photoionisation layer. For the analysed area there is a $\simeq$10-degree equatorward offset in magnetic latitude with respect to geographic latitude. At group ranges $r \leq 1,000$ km for several hours around the local noon the solar zenith angle is below 100°, so F-region heights are still illuminated by the Sun here. There are also some indication of the 2.0-hop F2 mode at $r \geq 2,400-2,500$ km. The noticeably lower elevation angle values and larger than expected $r^{min}[2.0F2] > 2r^{min}[1.0F2]$ in this region might be because this component is interacting with the ionospheric layer at comparatively higher latitudes where the maximum plasma frequency is lower due to lower values of the solar zenith angle.

The nighttime F2 echoes are represented by a 0.5-hop IS population. It is somewhat puzzling that maximum $\bar{\alpha}$ values occur near the local dawn at $\simeq 12$ UT ($\simeq 06$ MLT). The apparent absence of the respective nighttime 1.0-hop and 1.5-hop F2 echoes can be related to the relatively low ionospheric density that does not provide enough refraction for the HF rays to reach the curved Earth's surface over the horizon.

The nighttime 1-hop Es echo population has a diurnal maximum of $\bar{\alpha}$ before 06 UT (00 MLT). This result agrees with previous observations by nearby ionosondes showing that in winter the Es critical frequency maximises at around 04 UT (MacDougall et al., 2000).

4.2 Solar cycle variations

The seasonal/solar cycle variations of $\bar{\alpha}(r)$ for local midday at 10 MHz and 12 MHz are presented in Figure 7 (IS) and Figure 8(GS). The common feature in all panels is that, during the enhanced solar activity from 2012-2016, the maximum $\bar{\alpha}$ substantially increases while the respective r^{min} values decrease. This is expected as the higher f_p observed during solar maximum leads to stronger refraction, shifting echoes to higher elevation angle values at shorter group ranges. As we described in Subsection 4.1, the summer noon-time echoes during the solar maximum are dominated by the Pedersen mode, while the respective winter echoes are dominated by the low-angle mode. While both of these tendencies seem to be preserved during periods of low solar activity, the winter anomaly essentially disappears when the maximum which follows from the comparable maximum elevation angle values in summer and winter.

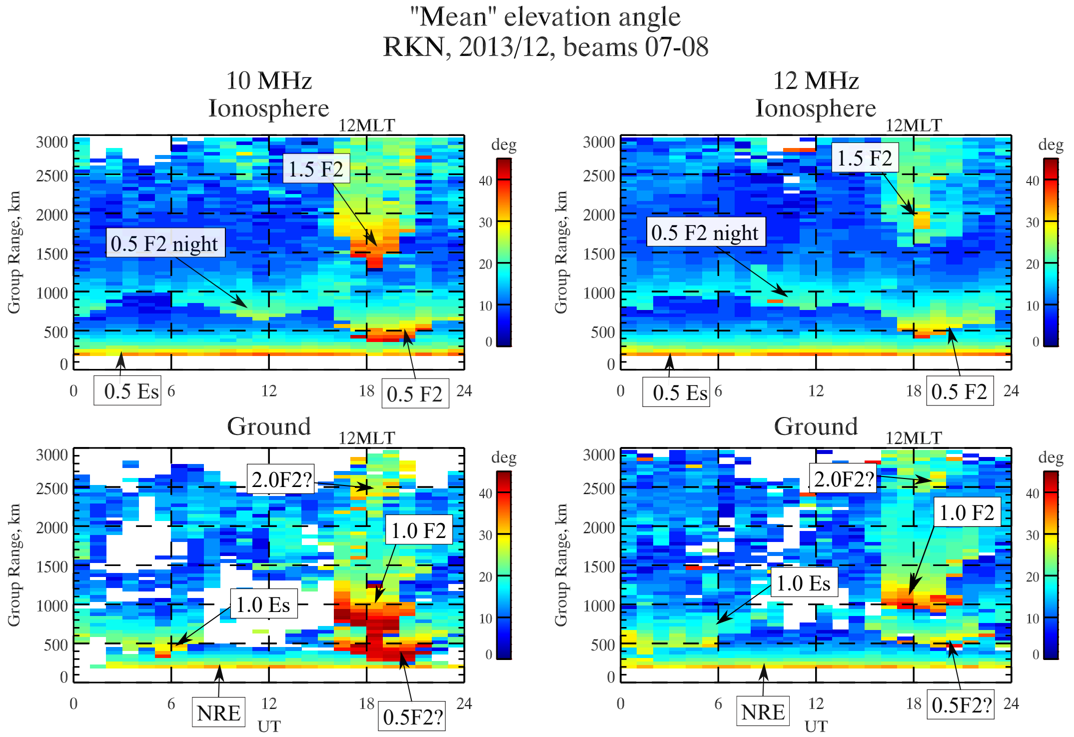

Figure 6. Group range-UT map of 'mean' elevation angle values $\bar{\alpha}$ (see Section 3 for details) in RKN beams 7-8 for December 2013.

5 Utilising elevation angle for characterising HF propagation characteristics

In this section we provide mathematical formalism and examples of using SuperDARN elevation angle to characterise HF propagation at high latitudes and estimate ionospheric parameters.

5.1 Ground range and virtual height

Virtual height h_v is an important parameter for determining ground range r_g of HF signals. In the conventional SuperDARN software, the virtual height is utilised in combination with the Breit and Tuve theorem to estimate the ground range of HF echoes (Chisham et al., 2008; Thomas & Shepherd, 2022). Following, e.g., (Chisham et al., 2008), the ground range of IS is calculated using:

$$r_g\left(r,\alpha\right) = R_E \sin^{-1}\left[\frac{r\cos\alpha}{R_E + h_v\left(r,\alpha\right)}\right], \tag{3}$$

where R_E is the Earth's radius. The existing conventional approaches assign a single value of elevation angle to each value of r. There are two main models implemented in RST, the 'standard model' based on a combination of fixed values of the virtual height for E and F layers and a more advanced empirical 'Chisham model' based on several years of elevation angle data from the SAS SuperDARN radar (Chisham et al., 2008). A recent model by Thomas and Shepherd (2022) represents an improved modification of Chisham model applicable to mid-latitude SuperDARN radars. Neither of these models accounts for local time, season, solar cycle, and geographic location. Furthermore, the assumption of a single propagation mode being observed in each range gate is not always applicable, as in reality multiple modes can be observed simultaneously at the same r. The

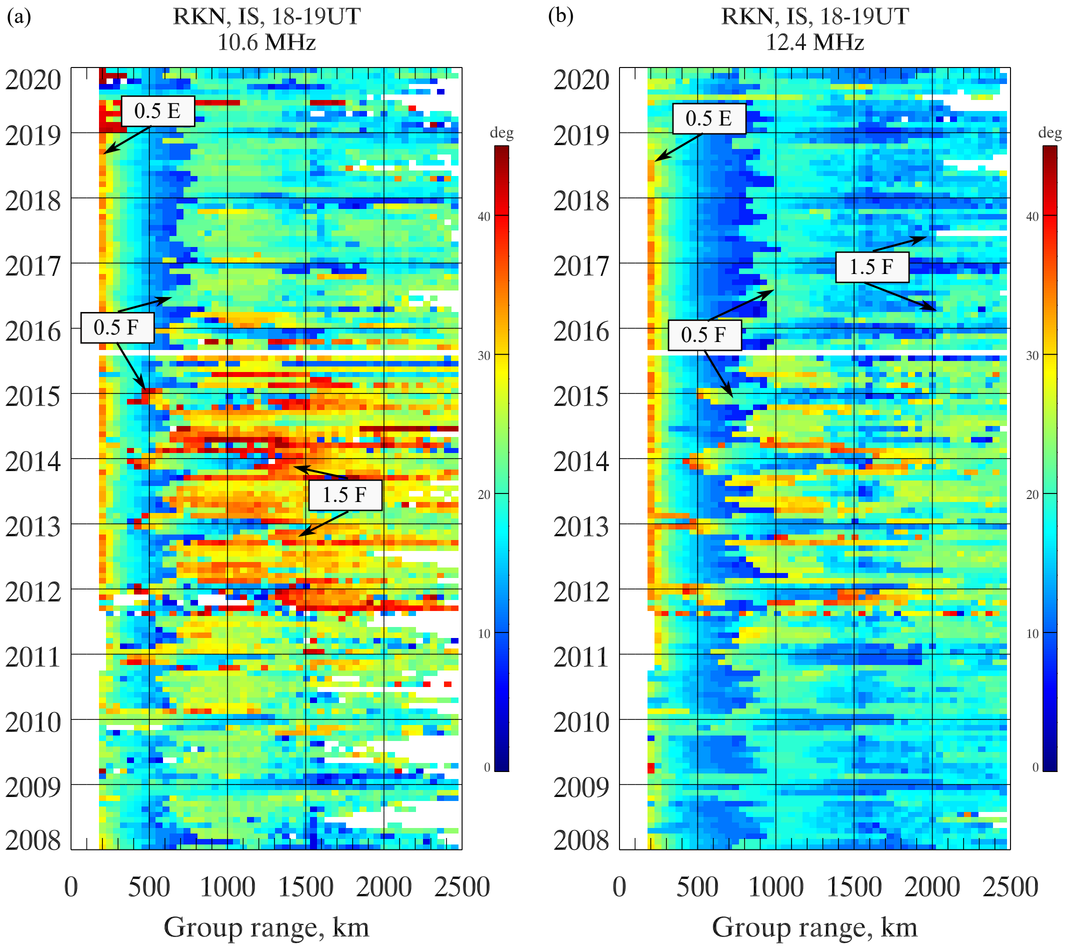

Figure 7. Monthly $\bar{\alpha}(r)$ values for IS during the solar cycle 24 at local noon for 10 MHz (a) and 12 MHz (b) frequency bands.

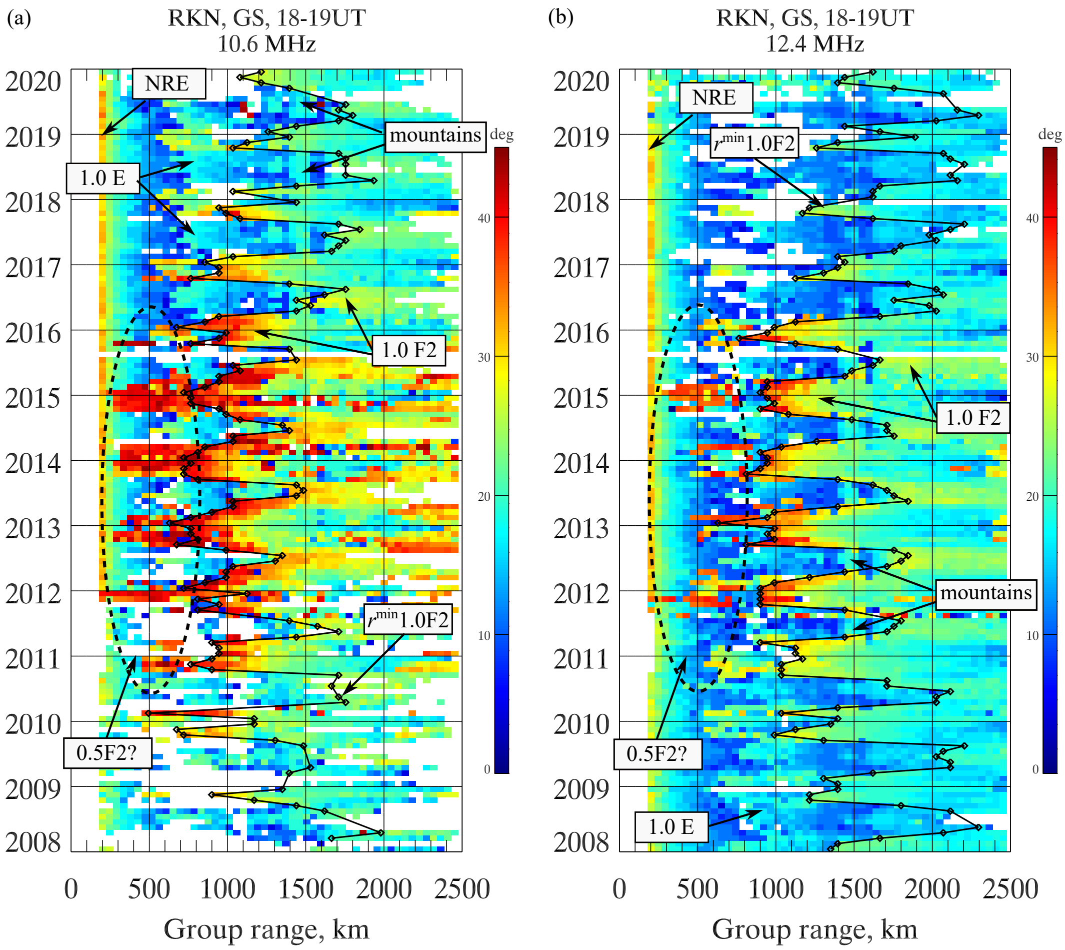

Figure 8. Same as Figure 7 but for GS. The solid black lines with diamonds show manually selected values of the skip zone group range r^{min} for 1.0-hop F2-layer mode. For details, see Section 5. The dashed black ellipses encircle 'leaked' 0.5-hop F2-layer IS component.

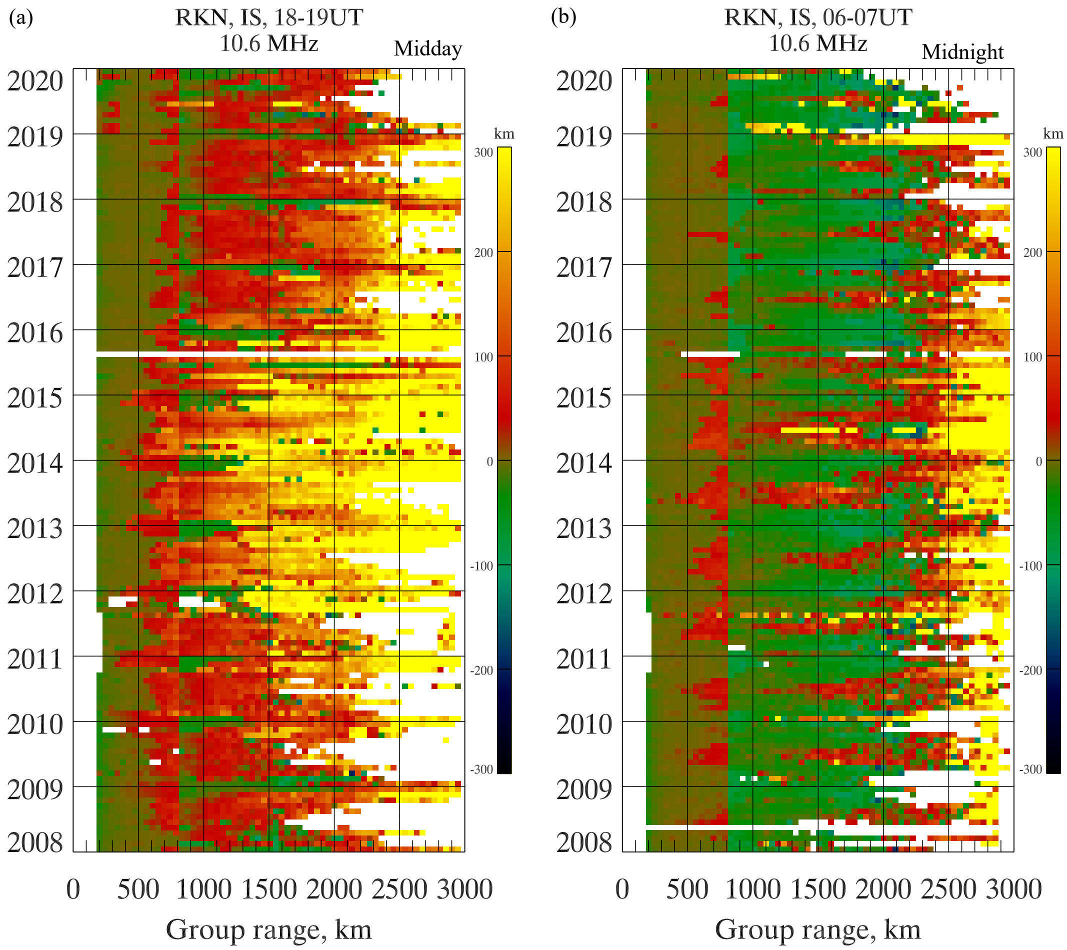

Figure 9. Deviation of the actual ground range estimates from Chisham range-finding model (Chisham et al., 2008) for 10 MHz for IS during the solar cycle 24 at local noon (a) and at local midnight (b).

availability of reliably calibrated elevation angle data for multiple radars allows SuperDARN to bypass these models by obtaining $h_v(r)$ directly from the observed data (Chisham et al., 2008) using the following expression:

$$h_v(r, \alpha) = \left(R_E^2 + r^2 + 2rR_E \sin\alpha\right)^{\frac{1}{2}} - R_E. \tag{4}$$

This approach can be extended to GS propagation by halving the group range in (4), thus providing the basis for direct estimation of the skip zone distance at the sounding frequency. This information can then be used to determine the conventional M-factors using, e.g., analytics from (Lockwood, 1983).

To illustrate areas where the conventional SuperDARN range-finding approach can be improved, in Figure 9 we show the difference between IS ground range values calculated using (i) the Chisham model (Chisham et al., 2008) and (ii) h_v obtained directly from the observed $\bar{\alpha}$ values (Equation 4). Red-yellow shading (positive values) corresponds to Chisham model values exceeding the observed values, and green shading (negative) corresponds to Chisham model values being less than observed values.

The sharp change at $r = 800$ km is related to the boundary between the E- and F-layer echoes, which is 'hardwired' into the Chisham model. From Figure 9 one can conclude that the model provides r_g values for E-layer returns ($r \leq 700$ km) that do not deviate much from the measurements. However, the conventional approach leads to significant biases in ground range of the IS radar returns from the F-layer, ($r > 700$ km), which on average are well in excess of the extent of a typical single SuperDARN range gate of 45 km. For daytime r_g is generally overestimated, and the errors increase with group range and maximise around the solar maximum. During nighttime the general situation reverses so that the model r_g values are mainly smaller than those observed experimentally while their solar cycle variation is not as strong as that observed during the daytime.

5.2 Plasma frequency

The electron density N_e represents the main characteristic of the ionosphere. It directly affects the propagation of HF radio waves, as the refractive index of the ionospheric plasma at $f \geq 10$ MHz is mainly determined by the plasma frequency $f_p \propto \sqrt{N_e}$ (Equation 2). It is possible to show that for IS in a spherically stratified ionosphere the plasma frequency can be determined from the following equation (e.g., Gillies et al., 2009):

$$f_p = f\sqrt{1 - \left[\frac{R_E}{R_E + h_s}\frac{\cos\alpha}{\sin\psi_B}\right]^2}, \tag{5}$$

where h_s is the height of the backscatter and ψ_B is the geomagnetic field inclination at the backscatter location. This dependence has been exploited in (Ponomarenko et al., 2011) to estimate the maximum plasma frequency of the F2 layer, f_{mF2}, using the IS Pedersen propagation mode identified through its nearly constant elevation angle *vs* group range.

Importantly, Equation 5 can also be applied to GS returns. For GS elevation angle can be used to determine plasma freqeuncy at the midpoint of the propagation path where the ray starts to 'bend' towards the Earth's surface. At this midpoint location, the ray becomes parallel to the ground, which is equivalent to $\sin\psi_B = \sin\pi/2 \equiv 1$. The scatter height h_s needs to be replaced with that of the 'reflection' height h_r (maximum altitude of the given ray). To illustrate the applicability of Equation 5 to GS, in Figure 10 we plotted results of numerical ray tracing using a realistic f_p profile consisting of Chapman-shaped E, F1 and F2 layers. The ionospheric parameters have been selected to approximate the conditions presented in Figure 2. The black solid line represents the input height profile $f_p(h)$, while the blue open circles show f_p values recovered from the elevation angle and the actual reflection height h_r obtained from the ray trajectories simulated for the radar frequency $f = 10$ MHz. As there is a one-to-one correspondence between f_p and α, by analogy with conventional ionosonde ionograms, it is possible to build 'elevation' ionograms $f_p[h_v(\alpha, r)]$. For the horizontally stratified ionosphere, the latter (black open circles in Figure 10) are equivalent to the conventional ionograms. In this case R_E approaches ∞, so that the dependence of f_p on h_s disappears from Equation 5.

In the case of oblique ionospheric HF propagation, the assumption that R_E approaches ∞ is not normally applicable, so there is a need to estimate h_r in some way. A simple replacement of h_r by h_v leads to a systematic overestimation of f_p, because h_v is intrinsically larger than the actual reflection/scatter height. To address this issue, we utilised the constant-height approach used in (Ponomarenko et al., 2011). This approach is based on the fact that the maximum heights of ionospheric layers lie within certain altitude intervals, and these intervals are relatively small with respect to the Earth's radius. This means that, without introducing large errors into estimating plasma frequency from Equation 5, we can assume h_r to be constant. To estimate the related errors, in Figure 11 we present the dependence of plasma frequency values recovered from elevation angle, $f_p[200 \leq h_r \leq 300]$ over a range of F2 layer heights between 200 and 300 km versus that calculated for the middle of the range, $f_p[h_r = 250]$. As seen in the figure, the error mag-

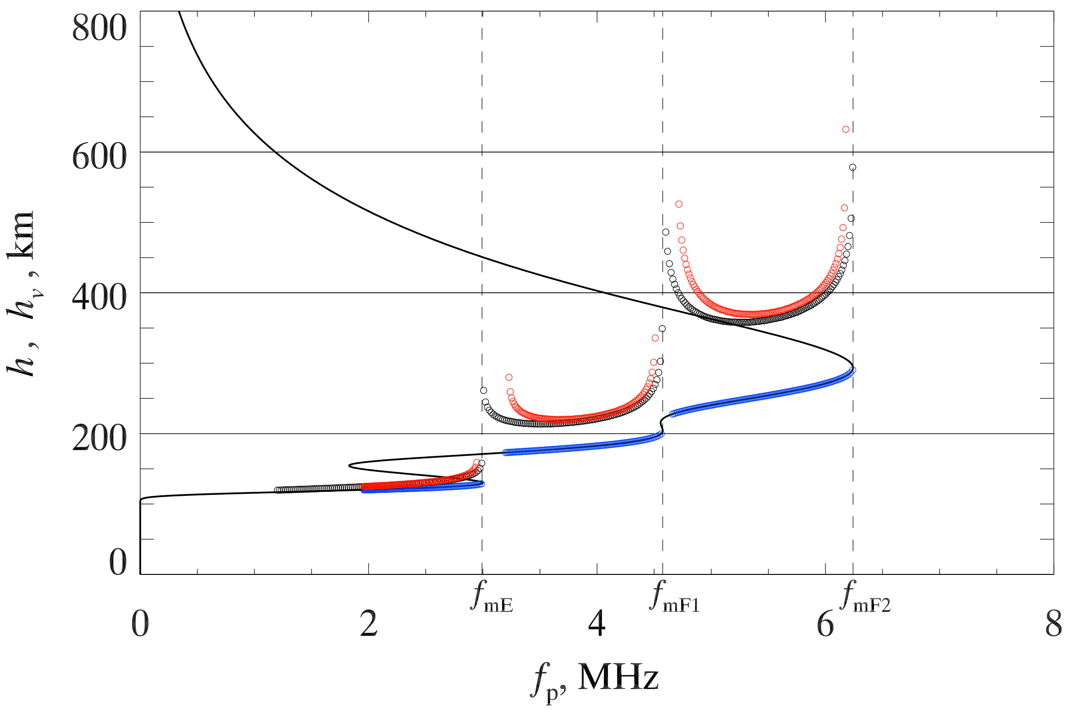

Figure 10. Results of ray tracing simulation for $f = 10$ MHz for a spherically stratified ionosphere. Black solid line represents an input height profile of plasma frequency, $f_p(h)$. Blue open circles show $f_p(h)$ values calculated using Equation 5 with actual reflection heights of the ground scatter echoes. Red open circles show dependence of plasma frequency on virtual height, $f_p(h_v)$, calculated using fixed v_r values for each ionospheric layer while black open circles correspond to an equivalent vertical ionogram for the same conditions (see text for more detail).

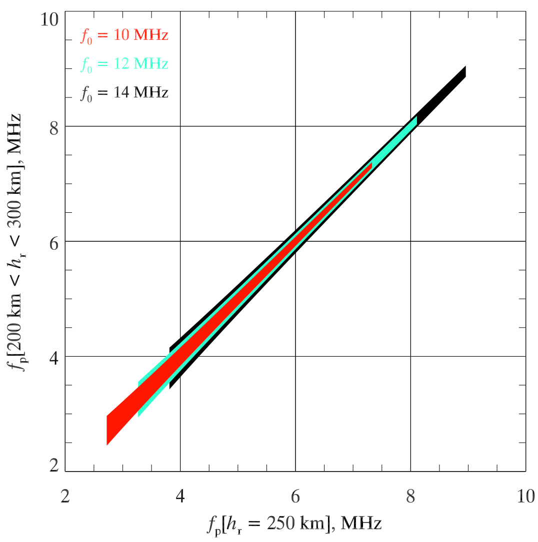

Figure 11. Errors in f_p values calculated using Equation 5 due to replacing the actual reflection height in 200 km $\leq h_r \leq$ 300 km by a fixed (mean) reflection height of $h_r = 250$ km. red, cyan and black areas correspond to f =10, 12 and 14 MHz, respectively.

nitude decreases from $\simeq \pm$250-350 kHz for the lowest f_p values to $\simeq \pm$50-100 kHz for the highest ones, both of which we consider to be acceptable. The red circles in Figure 10 represent the 'elevation ionogram' obtained from the ray tracing simulation with spherical geometry. In this case we used fixed values of h_r for E, F1 and F2 layers, and the respective components were identified based on the virtual height values:

- E layer ($h_v < 200$ km): h_r =120 km
- F1 layer (200$\leq h_v <$350 km): h_r =180 km
- F2 layer ($h_v \geq$350 km: h_r =250 km

While the resulting 'elevation ionogram' differs somewhat in shape from the conventional ionogram obtained by frequency-sweep vertical sounding, the reflection height approximation allows us to reproduce the critical frequencies for all three layers reliably.

5.3 Estimation of ionospheric propagation characteristics

To illustrate SuperDARN's ability to produce conventional HF propagation parameters, in Figure 12 we present a full solar cycle of monthly noon-time (18-19 UT) values of the F2-layer skip zone distance r_g^{skip}, as well as the respective plasma frequency f_p^{skip} and virtual height h_v^{skip} values corresponding to the midpoint of the skip zone ray for both frequency bands. These dependencies have been obtained from GS data using several steps:

1. The minimum group range for 1.0-hop F2 mode, r^{min}, has been identified visually from dependence of elevation angle on group range. The identification process is illustrated in Figure 4a where r^{min} is assigned to a sharp change in $\bar{\alpha}(r)$ coinciding with the left boundary of the 1.0-hop F2 population indicated by vertical red line. In Figure 8 the manually selected r^{min} values are shown by black lines with diamonds.
2. The virtual height of the skip zone boundary has been calculated from Equation 4 using $r = r^{min}/2$ (accounting for 1-hop ground scatter mode for which the group range is doubled as compared to that for ionospheric scatter from the same point) and the elevation angle value at the skip zone boundary, $\alpha^{skip} = \bar{\alpha}(r^{min})$ highlighted by horizontal red line in Figure 4a:
$$h_v^{skip} = \left(R_E^2 + \left(r^{min}/2\right)^2 + 2\left(r^{min}/2\right) R_E \sin\alpha^{skip}\right)^{\frac{1}{2}} - R_E. \tag{6}$$
3. The skip zone distance r_g^{skip} has been calculated using Equation 3 adjusted for 1.0-hop ground scatter mode (e.g., Thomas & Shepherd, 2022)
$$r_g^{skip} = 2R_E \sin^{-1}\left[\frac{(r^{min}/2)\cos\alpha^{skip}}{R_E + h_v^{skip}}\right]. \tag{7}$$
4. Finally, the plasma frequency at the reflection point of the skip zone ray has been calculated using Equation 5 adjusted to the 1-hop ground scatter mode (i.e., assuming that the ray at the reflection point propagates parallel to the Earth's surface, $\psi_B = \pi/2$)
$$f_p^{skip} = f\sqrt{1 - \left[\frac{R_E}{R_E + h_r(h_v^{skip})}\frac{\cos\alpha^{skip}}{\sin\pi/2}\right]^2}. \tag{8}$$
   Here the acual reflection height h_r was determined from the virtul height h_v^{skip} using the three-layer approximation described at the end of Subsection 5.2.

The skip zone distance (Figure 12a) maximises in summer and minimises in winter with lower frequency signals coming from closer ranges, as expected since ionospheric refraction increases with growing f_p/f ratio (Equation 1). As can be seen from Figure 3a, the

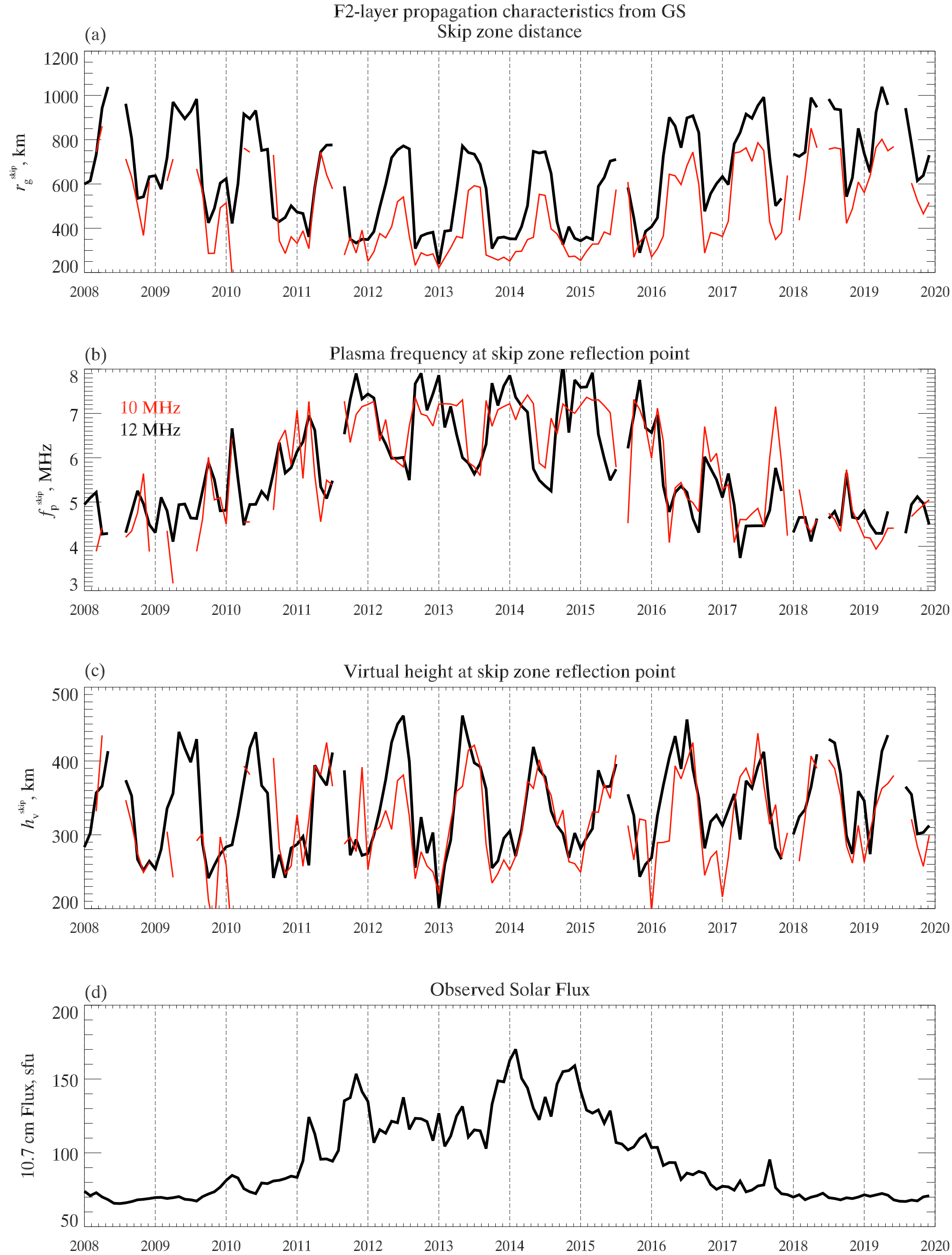

Figure 12. Monthly average 1.0-hop F2-layer propagation characteristics for 18-19 UT at two freqeuncy bands (panels (a)-(c), red – 10 MHz, black – 12 MHz) and 10.7 cm solar flux (panel (d)) over the solar cycle 24.

rays forming the skip zone boundary on the ground propagate along the separatrix between the Pedersen (red) and low-angle (green) rays, and these 'skip zone' rays are reflected in the vicinity of (just below) the ionisation maximum shown by the white dash line. This means that the estimated plasma frequency f_p^{skip} and virtual height h_v^{skip} can be treated as rough proxies of the critical frequency f_{mF2} and maximum virtual height of the layer. Within this approximation, f_{mF2} (Figure 12b) shows annual variations, with maximum values observed in winter due to the previously mentioned winter anomaly. This tendency is more pronounced around the solar maximum between 2011 and 2016. Both annual minimum and maximum f_{mF2} values increase around the solar maximum. The plasma frequency estimates in both frequency bands are very similar to each other, arguing for the robustness of our approach. Pronounced annual variations in h_v^{skip} (Figure 12c) between $\simeq 250-300$ km in winter and $\geq 400-450$ km in summer are synchronous with those in r_g^{min}, but they do not show any discernible solar cycle variation.

6 Summary and future directions

A statistical analysis of data from the RKN SuperDARN radar was performed. Elevation angle variations with range, time of day, season, and solar cycle activity were studied to establish the following properties of HF propagation modes at very high latitudes:

- F-layer modes
  - Summer daytime propagation in the F2 layer is dominated by the Pedersen (high-angle) mode, which is guided along a 'channel' in the vicinity of the F2 layer's maximum plasma density. This effect appears to be caused by the 'screening' of the low-angle F2 rays by a high density photoionisation E-layer, as well as by the F1-layer 'ledge'. During nighttime, the F2-layer propagation is dominated by low-angle modes because the presence of a semi-transparent Es-layer does not prevent the low-angle rays from reaching F-layer heights. The maximum nighttime elevation angle values are observed near the local dawn.
  - In winter, propagation near noon and midnight is dominated by the low-angle mode, as there is no regular photoionisaiton E-layer. Near solar maximum, the noon elevation angle values, and, therefore, electron density values, are significantly larger than the summer observations, reflecting the well-known *winter anomaly* when the winter daytime values of the F-layer plasma density are noticeably larger than those observed during the summer months (e.g., Yonezawa, 1971).
  - The GS F2-layer component can be strongly affected by echoes from mountain ranges, which produce separate continuous populations at fixed group ranges (see bottom right panel in Figure 2).
  - The F1-layer population seems to be apparent in the both IS and GS summer data (see top panels in Figure 2), when it supplements the regular E-layer in blocking the low-angle rays from penetrating to the F2-layer heights.
- E-layer modes
  - The photoionisation E-layer plays a significant role in summer daytime echo occurrence. Besides providing regular 0.5- and 1.0-hop low-angle E-layer modes, it also blocks the low-angle rays from reaching F-layer altitudes. The very high values of elevation angle for the 0.5-hop mode at the close ranges, which exceed those from the 1.0-hop mode, are most likely due to the semi-transparent Es-layers. Another potential cause for this effect can be contamination by the NRE whose occurrence maximises near the summer solstice (Ponomarenko et al., 2016). The summer nighttime E layer propagation is dominated by the Es-layer echoes.
  - In the winter, the photoionisation at E-layer heights disappears so that E-layer echoes are provided by sporadic layers, especially during nighttime. It is hard

to characterise the winter daytime E-layer echoes as they are obscured by the F-layer echoes, which move to close ranges due to the enhanced electron density caused by the winter anomaly.

- The near range echoes, in agreement with the previous observations, are abundant during the summer daytime. Their major effect is related to contamination of the E-layer echoes at very close ranges. While these echoes can be easily identified in GS due to a distinctly shorter group range as compared to 1.0-hop echoes, removing NRE from IS represents a significant challenge as they smoothly merge into the 0.5-hop E-layer echoes.

The solar cycle variations show the expected behaviour, as $\bar{\alpha}$ values for both IS and GS increase with enhanced solar activity levels, reflecting stronger refraction caused by the enhanced electron density.

We described in detail how the ionospheric propagation characteristics can be derived directly from observational data, thus bypassing an ionospheric model. The validity of this approach has been supported by a solar-cycle-long time series of monthly variations in the F2-layer maximum frequency, skip zone distance and virtual height of the layer's maximum, which showed the expected behaviour reflecting the known physical processes in the Earth's ionosphere.

SuperDARN elevation angle measurements can be used directly to produce reliable estimates of the ground ranges of SuperDARN echoes. This technique provides a viable alternative for the conventional range-finding algorithms in SuperDARN software, which tend to overestimate r_g for the F2-layer during the day and underestimate it at night.

In more general terms, SuperDARN estimates of f_{mF2} can be used to improve the reliability of models like E-CHAIM by filling spatial gaps between the existing CADI ionosonde observations. Furthermore, the spatio-temporal characteristics of the SuperDARN echoes constitute a robust database that can be used to characterise ground and ionospheric clutter in high-latitude HF surveillance systems like over-the-horizon radars.

This study has uncovered several technical and methodological issues that need to be addressed in the future. For example, the SuperDARN empirical criteria for classifying an echo as ground scatter may need to be improved, as there can be contamination of the GS echoes by IS echoes misidentified as GS, and *vice versa*. Another important problem to solve is that some propagation modes overlap statistically in group range. This introduces additional errors in characterising the propagation mode at a particular group range, as there may be more than one population present at a time. As an example, see group ranges 700-900 km in the top right panel of Figure 2 where the 0.5-hop F1-layer echoes overlap with the 'tail' of the 0.5-hop E-layer echoes. Another important issue is related to the conventional SuperDARN determination of the elevation angle, which restricts the maximum value of elevation angle to 40-45° due to the 2π phase ambiguity (see, e.g., Discussion and Conclusion section in (Ponomarenko et al., 2011)). This problem has been partially resolved in (Ponomarenko et al., 2016) by 'unwrapping' the interferometer phase data for NRE, but this approach still needs to be expanded to other propagation modes. Yet another problem is that in the current work we used a visual approach to identify different propagation modes, and at least some automation would be beneficial in processing large datasets. In that respect, Burrell et al. (2015) proposed an automatic technique for identifying propagation modes based on an empirical virtual height threshold. However, as one can see from our data in Figure 12, h_v can vary significantly depending on the season and the phase of the solar cycle, so this approach has to be implemented at a more systemic level accounting for these periodicities.

While the current work mostly focused on RKN data from central beams at local noon and local midnight, we plan to apply the same analysis to the other SuperDARN

Canada radars and include all local time sectors and beam directions. The resulting multi-year multi-radar database will be essential for building an empirical model of HF propagation at very high latitudes based directly on HF propagation data.

7 Open Research

Raw SuperDARN data used in this study together with the licensing information and data description are available from Federated Research Data Repository (FRDR), Canada, at (Super Dual Auroral Radar Network, 2021a, 2021b, 2021c, 2021d, 2021e, 2021f, 2021g, 2021h, 2021i, 2021j, 2021k, 2022).

The RAWACF data can be read using the Radar Software Toolkit (RST) written in C (SuperDARN Data Analysis Working Group, 2021).

Acknowledgments
PP is supported by GO Canada Grant G00024607 from the Canadian Space Agency. The authors acknowledge the use of SuperDARN data. SuperDARN is a collection of radars funded by the national scientific funding agencies of Australia, Canada, China, France, Italy, Japan, Norway, South Africa, United Kingdom and United States of America.

References

Bilitza, D. (2018). IRI the International Standard for the Ionosphere. *Advances in Radio Science*, *16*, 1–11. Retrieved from `https://ars.copernicus.org/articles/16/1/2018/` doi: 10.5194/ars-16-1-2018

Bland, E. C., McDonald, A. J., de Larquier, S., & Devlin, J. C. (2014). Determination of ionospheric parameters in real time using SuperDARN HF Radars. *Journal of Geophysical Research: Space Physics*, *119*(7), 5830-5846. Retrieved from `https://agupubs.onlinelibrary.wiley.com/doi/abs/10.1002/2014JA020076` doi: https://doi.org/10.1002/2014JA020076

Burrell, A. G., Milan, S. E., Perry, G. W., Yeoman, T. K., & Lester, M. (2015). Automatically determining the origin direction and propagation mode of high-frequency radar backscatter. *Radio Science*, *50*(12), 1225-1245. Retrieved from `https://agupubs.onlinelibrary.wiley.com/doi/abs/10.1002/2015RS005808` doi: https://doi.org/10.1002/2015RS005808

Burrell, A. G., Yeoman, T. K., Milan, S. E., & Lester, M. (2016). Phase calibration of interferometer arrays at high-frequency radars. *Radio Science*, *51*(9), 1445–1456. Retrieved from `http://dx.doi.org/10.1002/2016RS006089` (2016RS006089) doi: 10.1002/2016RS006089

Carbary, J. F. (2005). A Kp-based model of auroral boundaries. *Space Weather*, *3*(10). Retrieved from `https://agupubs.onlinelibrary.wiley.com/doi/abs/10.1029/2005SW000162` doi: https://doi.org/10.1029/2005SW000162

Chisham, G. (2018). Calibrating SuperDARN interferometers using meteor backscatter. *Radio Science*, *53*(6), 761-774. Retrieved from `https://agupubs.onlinelibrary.wiley.com/doi/abs/10.1029/2017RS006492` doi: https://doi.org/10.1029/2017RS006492

Chisham, G., Burrell, A. G., Marchaudon, A., Shepherd, S. G., Thomas, E. G., & Ponomarenko, P. V. (2021). Comparison of interferometer calibration techniques for improved SuperDARN elevation angles. *Polar Science*, *28*, 100638. Retrieved from `https://www.sciencedirect.com/science/article/pii/S1873965221000025` (SuperDARN / Studies of Geospace Dynamics - Today and Future) doi: https://doi.org/10.1016/j.polar.2021.100638

Chisham, G., Freeman, M. P., & Sofko, G. J. (2008). Mapping ionospheric backscatter measured by the SuperDARN HF radars – Part 1: A new empirical virtual height model. *Ann. Geophys.*, *26*, 823–841, www.ann-geophys.net/26/823/2008/. Retrieved from https://angeo.copernicus.org/articles/26/823/2008/ doi: https://doi.org/10.5194/angeo-26-823-2008

Chisham, G., Lester, M., Milan, S. E., Freeman, M. P., Bristow, W. A., Grocott, A., … Walker, A. D. M. (2007). A decade of the Super Dual Auroral Radar Network (SuperDARN): Scientific achievements, new techniques and future directions. *Surv. Geophys.*, *28*, 33–109. doi: 10.1007/s10712-007-9017-8

Davies, K. (1965). *Ionospheric radio propagation.* Washington: National Bureau of standards Monograph 80.

de Larquier, S., Ponomarenko, P., Ribeiro, A. J., Ruohoniemi, J. M., Baker, J. B. H., Sterne, K. T., & Lester, M. (2013). On the spatial distribution of decameter–scale subauroral ionospheric irregularities observed by SuperDARN radars. *Journal of Geophysical Research: Space Physics*, *118*(8), 5244-5254. Retrieved from https://agupubs.onlinelibrary.wiley.com/doi/abs/10.1002/jgra.50475 doi: https://doi.org/10.1002/jgra.50475

Gillies, R. G., Hussey, G. C., Sofko, G. J., McWilliams, K. A., Fiori, R. A. D., Ponomarenko, P. V., & St.-Maurice, J.-P. (2009). Improvement of SuperDARN velocity measurements by estimating the index of refraction in the scattering region using interferometry. *J. Geophys. Res.*, *114*, A07305. doi: 10.1029/2008JA013967

Greenwald, R. A., Baker, K. B., Dudeney, J. R., Pinnock, M., Jones, T. B., Thomas, E. C., … Yamagishi, H. (1995). DARN/SuperDARN: A global view of the dynamics of high-latitude convection. *Space Sci. Rev.*, *71*, 761-795.

Hughes, J. M., Bristow, W. A., Greenwald, R. A., & Barnes, R. J. (2002). Determining characteristics of HF communications links using SuperDARN. *Annales Geophysicae*, *20*(7), 1023–1030. Retrieved from http://www.ann-geophys.net/20/1023/2002/ doi: 10.5194/angeo-20-1023-2002

Lockwood, M. (1983). Simple M-factor algorithm for improved estimation of the basic maximum usable frequency of radio waves reflected from the ionospheric F-region. *IEE Proceedings F, Communications Radar and Signal Processing*, *130*(4), 296 – 302. doi: 10.1049/ip-f-1.1983.0049

MacDougall, J. W., Jayachandran, P. T., & Plane, J. M. C. (2000). Polar cap sporadic-E: part 1, observations. *J. Atm. Sol. Terr. Phys.*, *62*, 1155–1167. doi: 10.1016/S1364-6826(00)00093-6

Milan, S. E., Jones, T. B., Robinson, T. R., Thomas, E. C., & Yeoman, T. K. (1997). Interferometric evidence for the observation of ground backscatter originating behind the CUTLASS coherent HF radars. *Annales Geophysicae*, *15*(1), 29–39. doi: 10.1007/s00585-997-0029-y

Nishitani, N., Ruohoniemi, J. M., Lester, M., Baker, J. B. H., Koustov, A. V., Shepherd, S. G., … others (2019). Review of the accomplishments of mid-latitude Super Dual Auroral Radar Network (SuperDARN) HF radars. *Progress in Earth and Planetary Science*, *6*(27). doi: 10.1186/s40645-019-0270-5

Ponomarenko, P. V., Bland, E., & Kotyk, K. (2021). *White paper on FITACF3.* Retrieved 2022-10-10, from https://superdarn.github.io/dawg/files/sup_material/FITACF3_white_paper.pdf

Ponomarenko, P. V., Bland, E. C., McWilliams, K. A., & Nishitani, N. (2022). On the noise estimation in Super Dual Auroral Radar Network data. *Radio Science*, *57*(6), e2022RS007449. Retrieved from https://agupubs.onlinelibrary.wiley.com/doi/abs/10.1029/2022RS007449 (e2022RS007449 2022RS007449) doi: https://doi.org/10.1029/2022RS007449

Ponomarenko, P. V., Iserhienrhien, B., & St-Maurice, J.-P. (2016). Morphology and possible origins of near-range oblique HF backscatter at high and midlatitudes. *Radio Science*, *51*(6), 718–730.

Ponomarenko, P. V., Koustov, A. V., St.-Maurice, J.-P., & Wiid, J. (2011). Monitoring the F-region peak electron density using HF backscatter interferometry.

Geophysical Research Letters, *38*. doi: 10.1029/2011GL049675

Ponomarenko, P. V., Maurice, J.-P. S., Hussey, G. C., & Koustov, A. V. (2010). HF ground scatter from the polar cap: Ionospheric propagation and ground surface effects. *Journal of Geophysical Research*, *115*(A10). Retrieved from http://dx.doi.org/10.1029/2010JA015828 (A10310) doi: 10.1029/2010JA015828

Ponomarenko, P. V., Nishitani, N., Oinats, A. V., Tsuya, T., & St.-Maurice, J.-P. (2015). Application of ground scatter returns for calibration of HF interferometry data. *Earth, Planets and Space*, *67*(1), 138. Retrieved from https://doi.org/10.1186/s40623-015-0310-3 doi: 10.1186/s40623-015-0310-3

Ponomarenko, P. V., St.-Maurice, J.-P., & McWilliams, K. A. (2018). Calibrating HF Radar Elevation Angle Measurements Using E Layer Backscatter Echoes. *Radio Science*, *53*(11), 1438-1449. Retrieved from https://agupubs.onlinelibrary.wiley.com/doi/abs/10.1029/2018RS006638 doi: https://doi.org/10.1029/2018RS006638

Ponomarenko, P. V., St-Maurice, J.-P., Waters, C. L., Gillies, R. G., & Koustov, A. V. (2009). Refractive index effects on the scatter volume location and Doppler velocity estimates of ionospheric HF backscatter echoes. *Ann. Geophys.*, *27*(11), 4207–4219. doi: 10.5194/angeo-27-4207-2009

Ponomarenko, P. V., Waters, C. L., & Menk, F. W. (2007). Factors determining spectral width of HF echoes from high latitudes. *Ann. Geophys.*, *25*, 675-687. doi: 10.5194/angeo-25-675-2007

Ruohoniemi, J. M., & Baker, K. B. (1998). Large-scale imaging of high-latitude convection with super dual auroral radar network hf radar observations. *J. Geophys. Res.*, *103*, 20797-20811.

Super Dual Auroral Radar Network. (2021a). *SuperDARN 2008 RAWACF* [dataset]. Federated Research Data Repository. https://doi.org/10.20383/102.0454.

Super Dual Auroral Radar Network. (2021b). *SuperDARN 2009 RAWACF* [dataset]. Federated Research Data Repository. https://doi.org/10.20383/102.0453.

Super Dual Auroral Radar Network. (2021c). *SuperDARN 2010 RAWACF* [dataset]. Federated Research Data Repository. https://doi.org/10.20383/102.0448.

Super Dual Auroral Radar Network. (2021d). *SuperDARN 2011 RAWACF* [dataset]. Federated Research Data Repository. https://doi.org/10.20383/102.0451.

Super Dual Auroral Radar Network. (2021e). *SuperDARN 2012 RAWACF* [dataset]. Federated Research Data Repository. https://doi.org/10.20383/102.0451.

Super Dual Auroral Radar Network. (2021f). *SuperDARN 2013 RAWACF* [dataset]. Federated Research Data Repository. https://doi.org/10.20383/102.0449.

Super Dual Auroral Radar Network. (2021g). *SuperDARN 2014 RAWACF* [dataset]. Federated Research Data Repository. https://doi.org/10.20383/102.0452.

Super Dual Auroral Radar Network. (2021h). *SuperDARN 2015 RAWACF* [dataset]. Federated Research Data Repository. https://doi.org/10.20383/102.0447.

Super Dual Auroral Radar Network. (2021i). *SuperDARN 2016 RAWACF* [dataset]. Federated Research Data Repository. https://doi.org/10.20383/102.0446.

Super Dual Auroral Radar Network. (2021j). *SuperDARN 2017 RAWACF* [dataset]. Federated Research Data Repository. https://doi.org/10.20383/101.0289.

Super Dual Auroral Radar Network. (2021k). *SuperDARN 2018 RAWACF* [dataset]. Federated Research Data Repository. https://doi.org/10.20383/101.0290.

Super Dual Auroral Radar Network. (2022). *SuperDARN 2019 RAWACF* [dataset]. Federated Research Data Repository. https://doi.org/10.20383/102.0558.

SuperDARN Data Analysis Working Group. (2021). *SuperDARN Radar Software Toolkit (version 4.6)* [software]. Zenodo. Retrieved from https://doi.org/10.5281/zenodo.5156752 (Participating members: Schmidt, M.T., Bland, E.C., Thomas, E.G., Burrell, A.G., Coco, I., Ponomarenko, P. V., Reimer, A.S., Sterne, K.T., and Walach, M.-T.) doi: 10.5281/zenodo.5156752

Themens, D. R., Jayachandran, P. T., Galkin, I., & Hall, C. (2017). The Empirical Canadian High Arctic Ionospheric Model (E-CHAIM): NmF2 and hmF2. *Journal of Geophysical Research: Space Physics*, *122*(8), 9015-9031. Retrieved from https://agupubs.onlinelibrary.wiley.com/doi/abs/10.1002/2017JA024398 doi: https://doi.org/10.1002/2017JA024398

Thomas, E. G., & Shepherd, S. G. (2022). Virtual height characteristics of ionospheric and ground scatter observed by mid-Latitude SuperDARN HF radars. *Radio Science*, *57*(6), e2022RS007429. Retrieved from https://agupubs.onlinelibrary.wiley.com/doi/abs/10.1029/2022RS007429 (e2022RS007429 2022RS007429) doi: https://doi.org/10.1029/2022RS007429

Yonezawa, T. (1971). The solar-activity and latitudinal characteristics of the seasonal, non-seasonal and semi-annual variations in the peak electron densities of the F2-layer at noon and at midnight in middle and low latitudes. *Journal of Atmospheric and Terrestrial Physics*, *33*(6), 889-907. Retrieved from https://www.sciencedirect.com/science/article/pii/0021916971900894 doi: https://doi.org/10.1016/0021-9169(71)90089-4